# Effect of carrier dynamics on mode shift in the ultrafast timescale of perovskite microlasers *⊗*

Canpu Yang; Yuheng Liu; Wenjiang Tan ■ ( ); Jinhai Si ( ); Xun Hou



J. Chem. Phys. 162, 194705 (2025) https://doi.org/10.1063/5.0268133





# Articles You May Be Interested In

Different emissive states in the bulk and at the surface of methylammonium lead bromide perovskite revealed by two-photon micro-spectroscopy and lifetime measurements

APL Photonics (June 2016)

Excimer laser-A reliable tool for microprocessing and surface treatment

AIP Conf. Proc. (October 1993)

Individual contribution of electrons and holes to photocarrier-induced bandgap renormalization in intrinsic bulk GaAs

J. Appl. Phys. (September 2020)





# Effect of carrier dynamics on mode shift in the ultrafast timescale of perovskite microlasers

Cite as: J. Chem. Phys. 162, 194705 (2025); doi: 10.1063/5.0268133 Submitted: 27 February 2025 • Accepted: 28 April 2025 •







Published Online: 16 May 2025

Canpu Yang, Yuheng Liu, Wenjiang Tan, Dinhai Si, Dinhai

#### **AFFILIATIONS**

Key Laboratory for Physical Electronics and Devices of the Ministry of Education and Shaanxi Key Lab of Information Photonic Technique, School of Electronics and Information Engineering, Xi'an Jiaotong University, Xi'an 710049, China

a) Author to whom correspondence should be addressed: tanwenjiang@mail.xjtu.edu.cn

#### **ABSTRACT**

In semiconductor-based microlasers, the lasing performance and device properties are closely related to the behavior of the excited carriers. Comprehending their laser mechanisms and controlling laser behavior on ultrafast timescales is crucial. This paper employs a microscopic optical Kerr-gate method to investigate the lasing dynamic in a composite perovskite micro/nanostructure. The results show that the laser dynamics are influenced by bandgap renormalization and band-filling (BF) effects. At lower levels of pump fluence, the energy transfer process has the potential to impact the refractive index, resulting in a negligible transient mode shift. At higher levels of pump fluence, the observed extension of the stimulated radiation lifetime indicates the involvement of the hot carrier cooling process in laser emission. This mechanism facilitates the modulation of energy level occupancy states, resulting in a stable resonance wavelength during the initial few picoseconds. As the hot carriers cool, the BF effect can induce a notable change in the refractive index, leading to a redshift in the resonant modes. This study can offer insights into the lasing behavior driven by carrier dynamics and provide a promising strategy to regulate lasing performance in microcavity at ultrafast timescale.

Published under an exclusive license by AIP Publishing. https://doi.org/10.1063/5.0268133

#### I. INTRODUCTION

Humanity is rapidly advancing into the era of informatization and intelligence. Microelectronics technology is limited by the delay effects of circuit parameters, making it difficult to break through the nanosecond processing rate threshold. As a result, it gradually becomes unable to meet the requirements of modern information technology for low power consumption, high capacity, and high-speed transmission. Photons, due to their non-interfering and uncharged nature, can solve the delay dilemma and heat dissipation problems in device miniaturization without being limited by bottleneck blockages in transmission channels, making them an ideal information carrier for achieving picosecond ultrafast information processing speed.1 Coherent light source devices are one of the key components for achieving informatization in optoelectronic technology, which promotes the miniaturization of lasers. Micro/nano semiconductor lasers have the potential to integrate nanoscale photons and optoelectronic circuits, typically consisting

of a pump source, semiconductor gain medium, and resonant cavity. The pump source can pump electrons from ground states to excited states in the gain medium, providing energy for electron transitions. Under the action of appropriate energy photons, the gain medium emits coherent photons with the same characteristics as the incident light, including frequency, polarization, phase, and propagation direction, thus facilitating stimulated radiation. The gain medium is the core of micro/nano laser devices. Metal halide perovskites have emerged as competitive candidate materials for lasers due to their easy solution-processing chemical preparation and remarkable optoelectronic properties: high optical gain, flexible lasing wavelengths, superior fluorescence yield, and strong light-matter interactions.

Since the first amplified spontaneous emission (ASE) was obtained in perovskite films, 13 extensive research has been conducted on perovskite micro/nanolasers. Perovskite micro/ nanostructures with various morphologies were obtained based on different synthesis methods, including micro/nanowires, micro/

nanoplates, quantum dots, and thin films. These micro/ nanostructures serve as gain media and optical resonators for lasers. To create micro/nanolasers with low thresholds, high-quality factors, and excellent stability, researchers focus on optimizing the gain medium and modifying the cavity type. Liu et al. 14 prepared a hexagonal perovskite nanosheet array using the vapor deposition method, and the nanosheets have a periodic arrangement. By femtosecond laser pumping, low threshold (11 µJ/cm<sup>2</sup>), 0.64 nm full width at half maximum (FWHM), and high-quality factor (Q = 1210) were obtained. Xu et al. 15 reported a space consensus and advisory-supported crystallization process forming the seamless MAPbBr<sub>x</sub>Cl<sub>3-x</sub> perovskite arrays. This process achieves a high Q factor of 2915, and a threshold of 4.14 µJ/cm<sup>2</sup> is realized in whispering gallery mode (WGM) microcavity due to the ideal crystal pixel. Zhu et al.16 first reported a perovskite Fabry-Perot (F-P) mode laser, which exhibited a peak at FWHM of 0.22 nm at a pump energy density of 600 nJ/cm<sup>2</sup>, indicating laser formation. In addition, perovskite lasers with additional auxiliary cavities have also been studied. Wang et al. 17 achieved inorganic perovskite vertical-cavity surface-emitting lasers (VCSEL) nanocrystals by hot injection method and spin-coated on distributed Bragg reflector (DBR) mirrors, resulting in a low-threshold multicolor laser (9 μJ/cm<sup>2</sup>). Goldberg et al. 18 proposed a fully solution-processed method to fabricate external Distributed Feedback (DFB) gratings on MAPbI<sub>3</sub> waveguides, yielding DFB lasers with narrow line widths (<0.2 nm) and strong polarization.

In addition to the morphology and structure of microcavities, the laser performance is closely related to photoinduced carrier dynamics, particularly the processes of carrier excitation, hot carrier relaxation, and electron-hole recombination. Since these processes occur on the timescale of femtosecond-to-nanosecond, directly measuring the intrinsic relationship between photogenerated carrier dynamics and device parameters is challenging. Femtosecond time-resolved photoluminescence (TRPL) and femtosecond transient absorption (TA) techniques are employed to explore the carrier behaviors involved in the emission process. Some researchers have conducted extensive analyses of the laser characteristics of perovskite microcavities in both the time and spectral domains. Schlaus et al. 19 revealed the blueshift of the gain region within 25 ps, a signature of plasma-coupled laser emission, which determines the underlying mechanism in a single nanowire laser. Wang et al.<sup>20</sup> studied the bathochromic shift of a single microporous plate under high pump fluence. They effectively removed the mode shift by employing DBR mirrors, optimizing the mode quality of the microlaser. Du et al.<sup>21</sup> found the high Q factor single-mode lasers from perovskite microspheres. Through temperature-dependent PL spectroscopy, TRPL technology, and Raman spectroscopy, it has been confirmed that the lasing mechanism transitions from exciton scattering to exciton-phonon scattering as the temperature increases from 77 to 300 K. Weng et al.<sup>22</sup> observed an adverse move of the gain profile attributed to the bandgap renormalization (BGR) effect and provided extensive insight into the laser micro-mechanism and hot carrier process in microplates. He et al.<sup>23</sup> utilized TRPL technology to investigate not only the laser attenuation curve characteristics of spectral integration under different pump fluences in CsPbBr<sub>3</sub> nanowires but also the temporal dependence of laser spectra. Ma et al.24 employed the TA and TRPL technologies, and the results demonstrated that the band-filling (BF) effect can cause a significant change in the refractive index of the perovskite nanowires, resulting in an unfavorable redshift and broadening of the resonant modes. Su et al.<sup>25</sup> reported CsPbBr<sub>3</sub> microcavities with different kinds of morphology. The fast decay lifetime and slow decay lifetime, measured by TRPL, are attributed to stimulated lasing emission and spontaneous emission, respectively. He et al.26 successfully constructed a low laser threshold (22 µJ/cm<sup>2</sup>) composed of CsPbBr<sub>3</sub> nanocrystalline thin film and DBR; the single-mode VCSEL was used to investigate the carrier dynamics through pump-dependent TRPL measurements. He et al.<sup>27</sup> measured the TRPL at 20 K to study the many-body excitonic interactions in 2D lead-halide perovskites and offer a vision to expand the field of solution-processed multicolor lasers. Polimeno et al. 28 used TRPL measurements to identify blueshift observed above the threshold, a unique phenomenon resulting from strong coupling between excitons and confined optical modes in the perovskite crystal.

In this paper, CsPbBr3 nanowires and the nanowire + microplate composite are synthesized by a one-step synthesis method, and the micro/nano laser is achieved by femtosecond laser pumping. Then, femtosecond-resolved optical Kerr-gate (OKG) technology is employed to explore the laser dynamics in the composite to reveal the relationship between laser performance and carrier dynamics. Meanwhile, femtosecond TA technology can help detect the carrier behaviors involved in the emission process. First, one explores the threshold of the individual nanowires with F-P laser resonant mode and the mode variation with pump fluence. Then, the nanowire + microplate composite is employed to explore the pump fluence and time-resolved laser dynamic. It is worth noticing that the BGR and BF effects are revealed to affect the laser performance. The obtained results demonstrated that BF can affect the absorption coefficient at high levels of pump fluence. The energy transfer and the hot carrier cooling processes can affect the transient refractive index change, resulting in a slight redshift of resonant modes. Exploring carrier dynamics characteristics of the composite microstructure can provide an effective strategy for optimizing the perovskite micro/nanolaser.

#### II. METHOD

#### A. Synthesis of CsPbBr<sub>3</sub> perovskite microstructures

The CsPbBr<sub>3</sub> microplates and nanowires were synthesized with well-defined morphologies formed on the substrate through a one-step chemical reaction using a solution method. Specifically, 0.25 mmol of CsBr and 0.25 mmol of PbBr<sub>2</sub> powder were dissolved in the dimethyl sulfoxide (DMSO) solvent to prepare precursor solutions. Next, a sample holder containing 30 ml of dichloromethane (DCM) was added to the reaction vessel, and the substrate was placed on the sample holder. Take 1  $\mu$ l of solution from the precursor solution and drop it onto the substrate. Place it in a constant temperature box at 60  $^{\circ}$ C in a DCM atmosphere for 5 h. Finally, the sample was dried in a vacuum oven.

# **B.** Optical measurement

In the homemade femtosecond-resolved OKG fluorescence spectroscopy measurement system (see Fig. S1, supplementary material), a titanium-doped sapphire femtosecond laser (Coherent Inc., USA) was employed as the laser source of the system. The

output laser center wavelength is 800 nm, the repetition frequency is 1 kHz, the pulse width is 50 fs, and the output power is 5 W. The β-barium borate (BBO) crystal generated a 400 nm excitation beam and focused the sample to excite photoluminescence using an objective lens (40-x, NA = 0.75). Photoluminescence was focused on an optical Kerr medium with gating pulses after transiting a linear polarizer. Thus, the polarization rate of the photoluminescence pulse changes; part of the beam was transmitted through optical fibers. By adapting the delay time (optical path) between the gating pulse and the photoluminescence pulse, a TRPL spectrum was recorded using a spectrometer. To avoid the problem of switching time broadening caused by the walk-off effect,<sup>29</sup> the thickness of 1 mm optical Kerr medium was selected here. In addition, OKG technology is an ideal tool for studying laser dynamics due to its ultrafast time resolution (see Fig. S2, supplementary material) and implementation of wide-spectrum measurements. In the homemade fs- TA microscopy system (see Fig. S3, supplementary material), the titanium-doped sapphire femtosecond laser had identical specifications as described above. First, the light source was separated into two paths by a beam splitter; the first beam was employed to excite a BBO crystal (generate the second harmonic), and the second beam (as the probe light) was centered onto sapphire to yield white light supercontinuum by self-phase modulation. Then, the probe light and pump light were centered on the perovskite material using a 40-x objective lens (overlapped spatially through a dichroic mirror). The TA spectra can be observed by adjusting the delay time between the pump and probe signals.

#### **III. RESULTS AND DISCUSSION**

CsPbBr3 micro/nanostructures were synthesized using a onestep chemical reaction using a solution method, as shown in Fig. S4(a) (supplementary material). To demonstrate the nature of CsPbBr3 micro/nanostructures, x-ray diffraction (XRD) measurements were performed, as shown in Fig. S4(b) (supplementary material). Two main peaks appeared at 15.26° and 30.77° indexed to the (100) and (200) crystal planes, respectively. It can be found that the diffraction peak has a high intensity and a narrow halfwidth without the appearance of many miscellaneous peaks. Therefore, it can be concluded that the high-quality growth of CsPbBr<sub>3</sub> micro/nanostructures and the relatively pure phase structure. The optical properties of the samples were further investigated. Photonic lasing was attributed to the unique ability of the nanowire to simultaneously function as both a laser cavity and a gain medium.<sup>3</sup> The nanowire morphology defines the laser cavity, bounded by its end facets. A homemade micro-region PL device was equipped with a femtosecond laser source to study the optical characteristics of the individual nanostructure, including photoluminescence and laser properties. The investigated nanowire is shown in Fig. 1(a), it is ~9 µm long and has a diameter around 800 nm. When the pump fluence is under the lasing threshold, the emission spectrum shows a broad peak of about 520 nm at room temperature. It is apparent that the luminescence of the individual nanowire exhibits a Gaussian distribution [see Fig. 1(a)], with an FWHM of ~20 nm, close to the fluorescence performance with the reported CsPbBr<sub>3</sub> nanostructures.<sup>31</sup> This spontaneous emission is primarily attributed to the excitonic states of CsPbBr3 nanostructures, due to

the exciton binding energy exceeding the thermal energy at room temperature. 32,33

To measure the laser characteristics of individual nanowires, the size of the laser beam was optimized by adjusting the space between the microscope objective and the sample. We used defocused excitation to ensure that the entire sample was uniformly excited and not damaged by a femtosecond laser. The representative emission spectrum of the individual CsPbBr3 nanowire at room temperature with pump fluence (pulse energy per unit area) is shown in Figs. 1(b) and 1(c). When the pump fluence exceeds the laser threshold, strong light is generated on both ends of the nanowire (see Fig. S5, supplementary material). With the pump fluence rising, a sharp emission peak comes out and sharply increases in the lowenergy band tail compared with spontaneous emission. The strength is several orders of magnitude heightened with fluorescence, indicating that the lasing from the nanowire. For the excitation exceeding the threshold, different laser modes are noted from mode A to mode C, relating to the emission of photon energy from high to low. The laser modes are allocated to the longitudinal modes of the cavity specified by the nanowire surfaces at both ends. The dependence of output strength and FWHM with pump fluence is shown in Fig. 1(b). The "S-shaped" light output-light input behavior yields a laser threshold of  $\sim 17.5 \,\mu\text{J/cm}^2$ , and the sudden drop in the FWHM confirms lasing generation.

Further research was conducted on the laser performance of CsPbBr3 nanowires with different lengths. In theory, the Free Spectrum Range (FSR) of nanowire resonators, i.e., the axial mode spacing  $(\Delta \lambda)$ , is estimated with the formula:  $\Delta \lambda = \lambda^2/(2 N_{eff} L)$ , where  $N_{eff}$  is the effective refractive index of the nanowire, L is the length of the nanowire, and  $\lambda$  is the resonant wavelength. From the resonant wavelengths of nanowires of various lengths above the lasing threshold shown in Fig. S5 (supplementary material), as the nanowire length increases from 7.796 to 12.253  $\mu$ m, the mode spacing decreased from 2.23 nm to ~1 nm. Through linear fitting, it was found that a linear relationship happens between the mode spacing and the reciprocal of the nanowire length, which proves the formation of F-P cavities [see Fig. S6(a), supplementary material]. The spontaneous emission coupling factor ( $\beta$ ) can be conveniently employed to explain why laser intensity and coherence show intense enhancement around the threshold.<sup>34–36</sup> Meanwhile,  $\beta$  (0.18) can be calculated by the ratio of the difference in emission intensity before and after reaching the threshold, as shown in Fig. S6(b) (supplementary material). Then, one observes the intensity changes and mode shifts of different modes through variable pump excitation. As shown in Fig. 1(c), the same laser mode will transfer to higher photon energy as the pump fluence increases. One plotted the intensity and peak positions of the individual nanowire laser modes as a function of the pump fluence in Figs. S7 and S8 (supplementary material). As the pump fluence increases, the entire gain spectrum undergoes a redshift, indicating that the BGR effect intensifies with the increasing carrier density. The bandgap shrinkage phenomenon in the BGR effect is caused by the multibody effect under high carrier density.<sup>37</sup> On the other hand, all modes exhibit a blueshift of 0.5-1 nm, which is due to a higher injected carrier density reducing the refractive index in CsPbBr3, resulting in a blueshift of the single resonant mode, consistent with previous observations in CsPbBr<sub>3</sub>. <sup>19,23</sup>

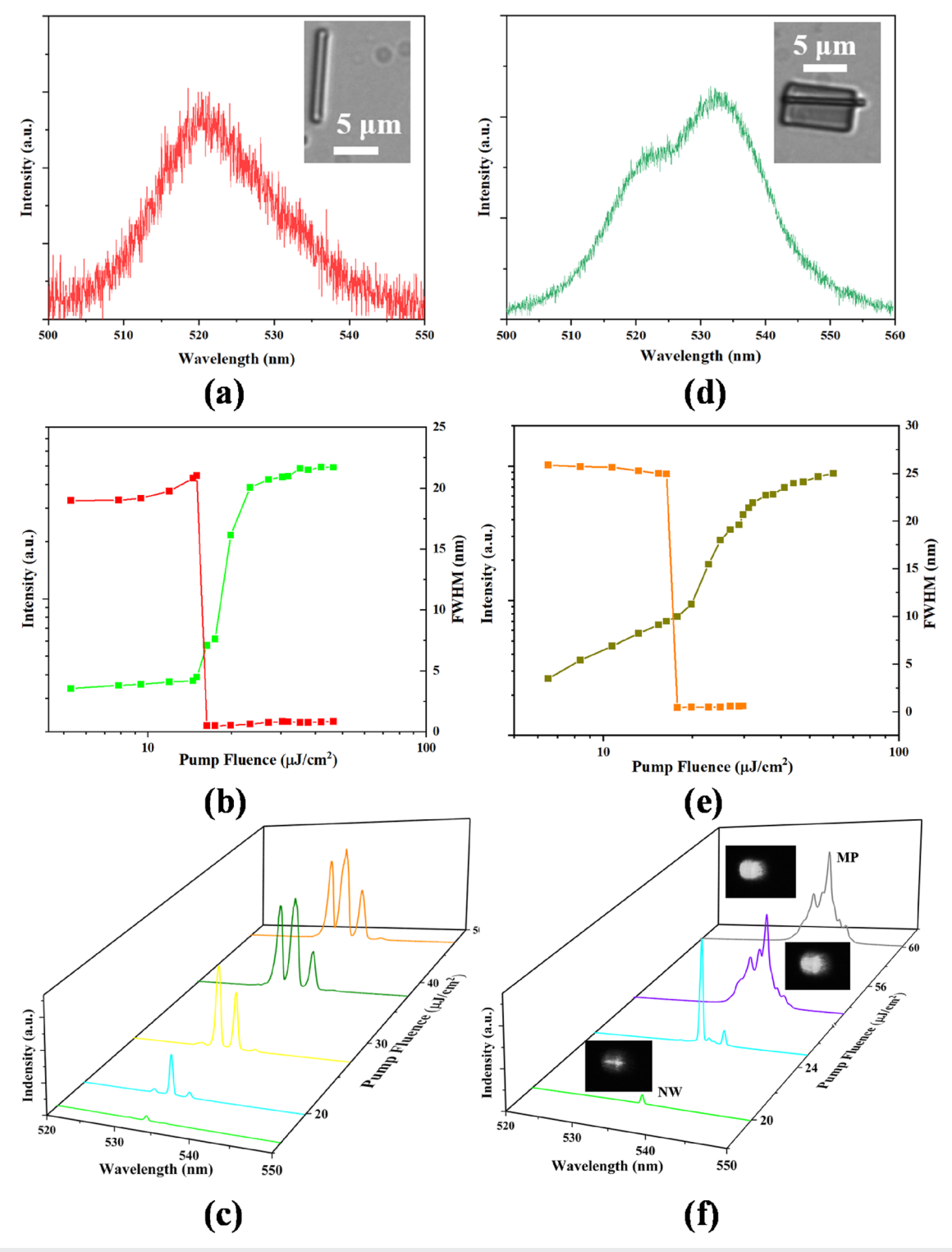


**FIG. 1.** (a) Photoluminescence spectra of the nanowire. Insert: Optical microscope images of the fabricated CsPbBr $_3$  perovskite nanowire. Scale bar, 5  $\mu$ m. (b) Evolution of integrated emission intensity and FWHM as a function of pump fluence. (c) Emission spectra of individual CsPbBr $_3$  nanowire as a function of pump fluence. (d) Photoluminescence spectra of the composite. Insert: Optical microscope images of the composite. Scale bar, 5  $\mu$ m. (e) Evolution of integrated emission intensity and FWHM as a function of pump fluence. (f) Emission spectra of the composite as a function of pump fluence. NW: nanowire resonance mode. MP: microplate resonance mode.

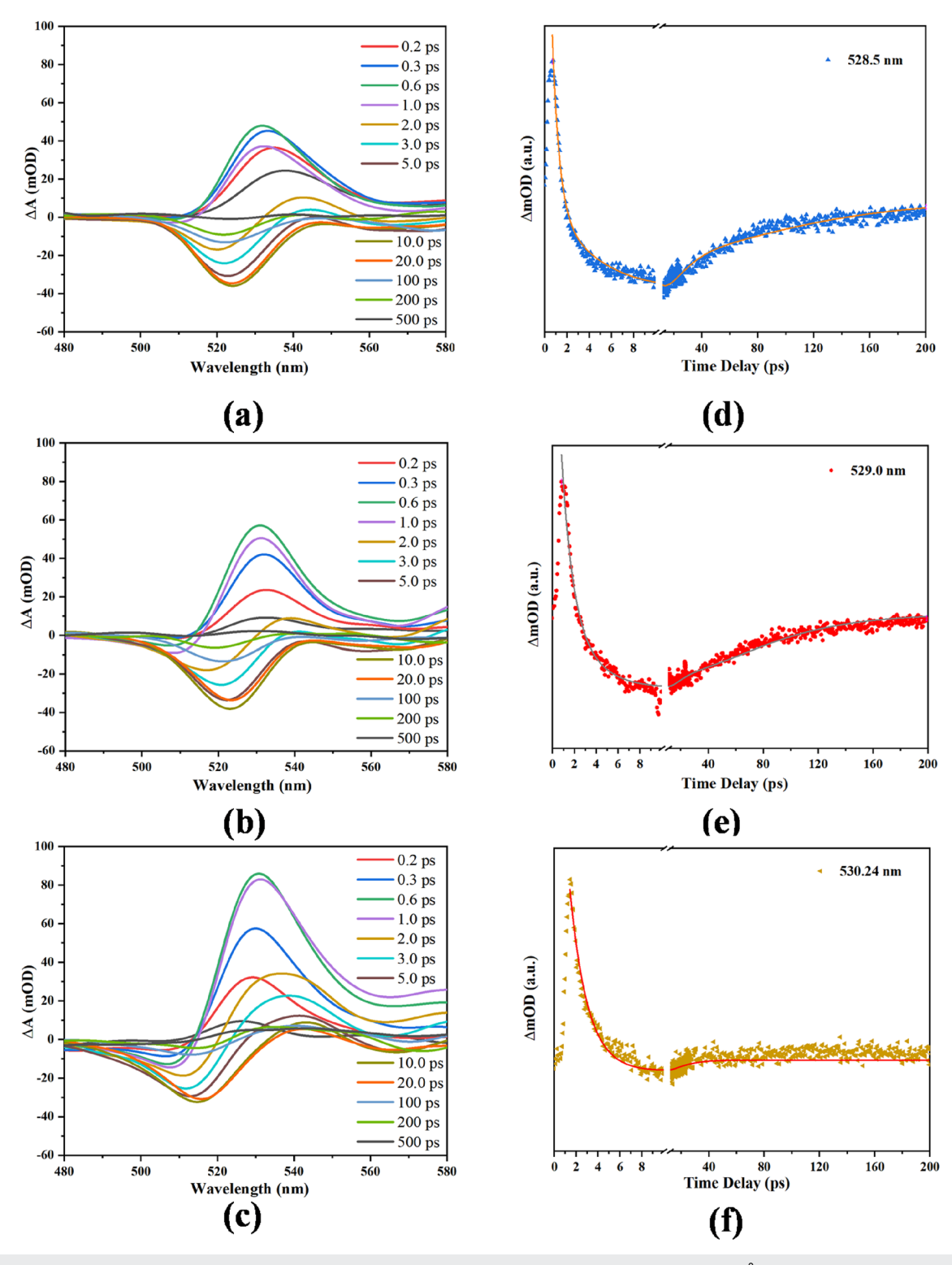
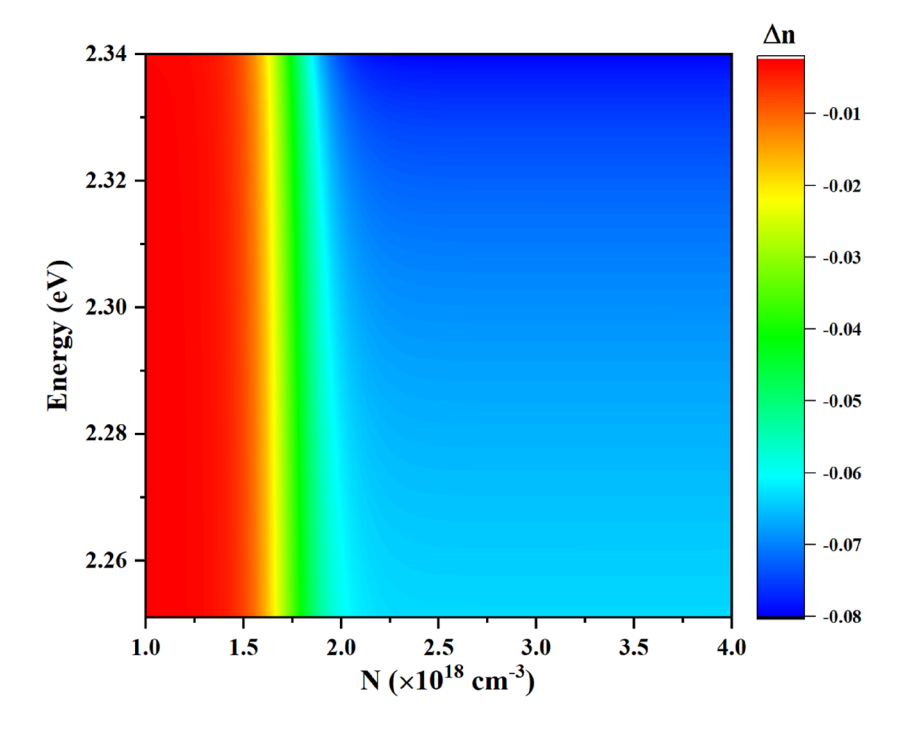


FIG. 2. (a)–(c) TA spectra (smoothed) with different delay times from 0.2 to 500 ps with pump fluences of 22.8, 32.7, 53.7  $\mu$ J cm<sup>-2</sup>, respectively. (d)–(f)  $\Delta$ A~ delay traces of CsPbBr<sub>3</sub> composite within the first 200 ps at different probe wavelengths of PA signals. The solid lines represent the fittings to experimental data with an exponential sum function.

To investigate the evolution of laser emission dynamics in the nanowire and microplate structure, we analyzed a composite system that demonstrates a sequential laser emission, where the nanowire emits first, followed by the microplate, as the pump fluence rises. The structure of the nanowire + microplate composite is shown in Fig. 1(d). The size of the laser beam size was optimized to ensure consistent excitation upon the composite structure. The emission spectrum is shown in Fig. 1(d), and the luminescence of the visible composite has two distinct emission peaks at around 520 nm and around 533 nm with an FWHM over 25 nm. As the pump fluence increases, a sharply stimulated emission peak comes out, with an intensity several orders of magnitude higher than that of spontaneous emission, indicating the lasing from the composite structure. The dependence of the output intensity and FWHM on pump fluence are shown in Fig. 1(e), and it can be concluded that the lasing threshold is  $\sim 17.5 \,\mu\text{J/cm}^2$ . The narrow FWHM occurred at around 536.5 nm considered the nanowire resonant mode. 38-40 Then, the resonant mode of the microplate (\$\sigma 539.5 \text{ nm}) appears and dominates as pump fluence increases. From the simulated results by COMSOL software in Fig. S9 (supplementary material), it can be seen that the mode distribution of the nanowire is mainly at higher photon energies compared to the microplate, which is consistent with the observed laser image [see Fig. 1(f)].

Furthermore, the carrier process of the composite urgently needs to be clarified. Typically, two factors can affect the bandgap features of inorganic perovskite: the BF and the BGR effects. When the nanostructure is excited by a laser pulse, the filling of hole states and electron states in the valence band and the conduction band can lead to the bleaching of optical inter-band transitions. The BF effect explains that photoexcited carriers cool down to the band edge and occupy the finite states on account of the Pauli exclusion principle, thereby suppressing band-edge absorption.

TA spectroscopy can be implemented to study the excited carrier species in the CsPbBr3 composite. To analyze TA spectra accurately, one concentrated the carrier process from 0.2 to 500 ps delay time in Figs. 2(a)-2(c). The features of the two signals are as follows: (1) A photo-induced absorption (PA) signal in a low energy region can be considered as a fingerprint due to the BGR process. 43 When the perovskite material is excited by photons, the free carrier species rise, leading to enhanced Coulombic interactions among them, resulting in band-gap shrinkage, thereby the increased absorption of the probe photons.<sup>44</sup> (2) One feature is the negative signal into the photo-induced bleaching (PB) of the ground state since the comparable peak is near the band gap of the CsPbBr<sub>3</sub> material. One further explores the TA spectra at different pump fluences and various delay times to study fluence- and time-dependent performances of the PA and PB signals. First, a bathochromic shift can be seen in the PB peak within 0-10 ps. This is also a powerful testimony to the appearance of the BGR effect. 22,45 Due to the relatively high carrier density above the threshold, the BF effect plays a significant role in the ultrafast process. It can be seen that the maximum PB peak became few changed when the pump fluence increased from low to medium; however, the blueshift happened in the PB peak when the pump fluence came to a high value. Such a phenomenon demonstrated that the BGR and BF effects have quite a high contribution to the bandgap features at the low to medium pump fluence, and the BF effect becomes dominant as the carrier density increases under high fluence, thereby mitigating the influence of the BGR process. Then, one offers a phenomenological model to suit the gauged PA signal quantitatively and concentrates the dynamic arguments as follows:  $y = A^* \exp(-\frac{t}{\tau_1})$ +  $(1 - \exp(\frac{t}{T}))^* (B^* \exp(-\frac{t}{\tau_2}) + C^* \exp(-\frac{t}{\tau_3}))$ , where the first exponential term denotes the BGR effect and the second part describes the fast recombination and slow recombination; A, B,



**FIG. 3.** The simulation results of the refractive index change as a function of carrier density and photon energy, considering the BF and BGR effects.

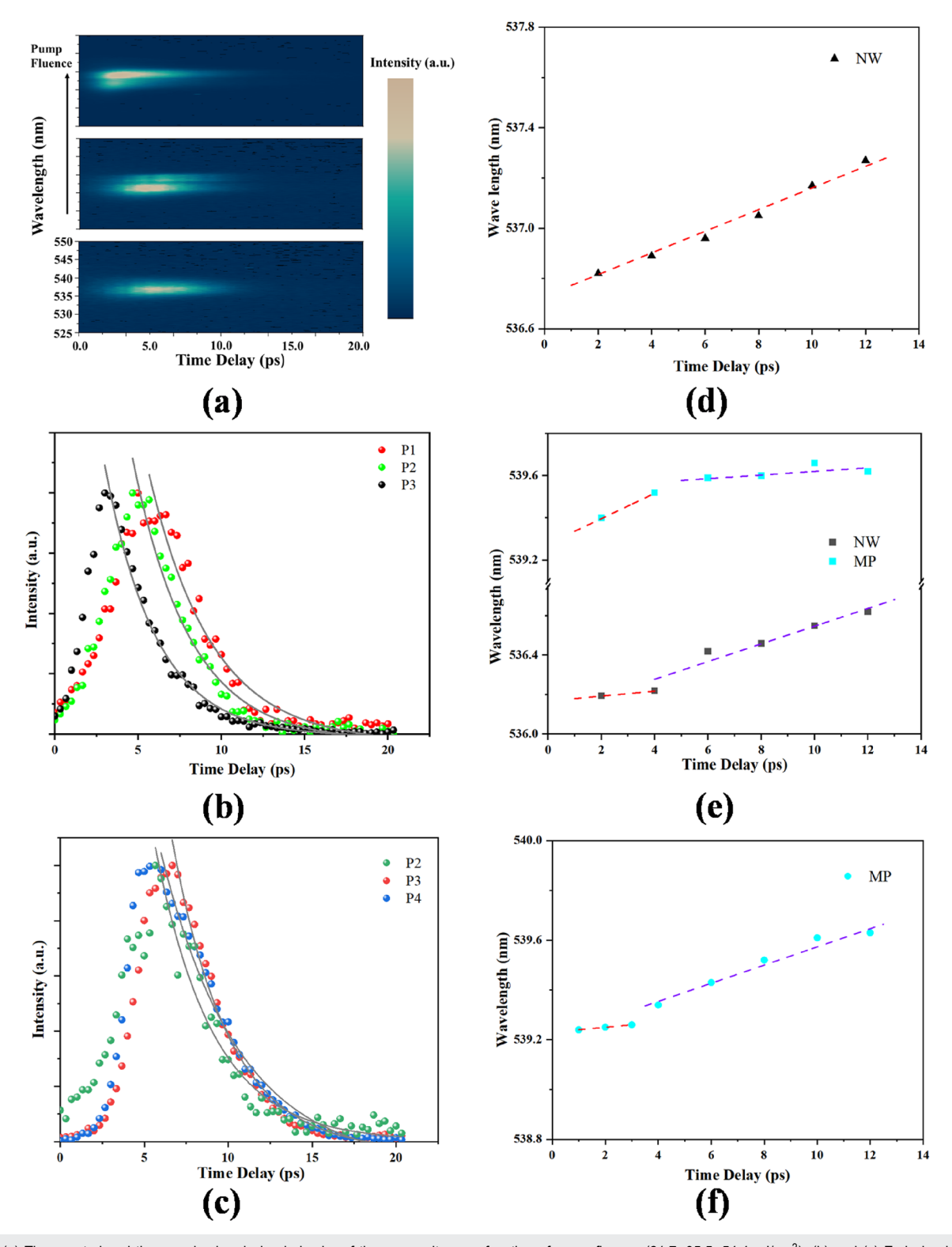
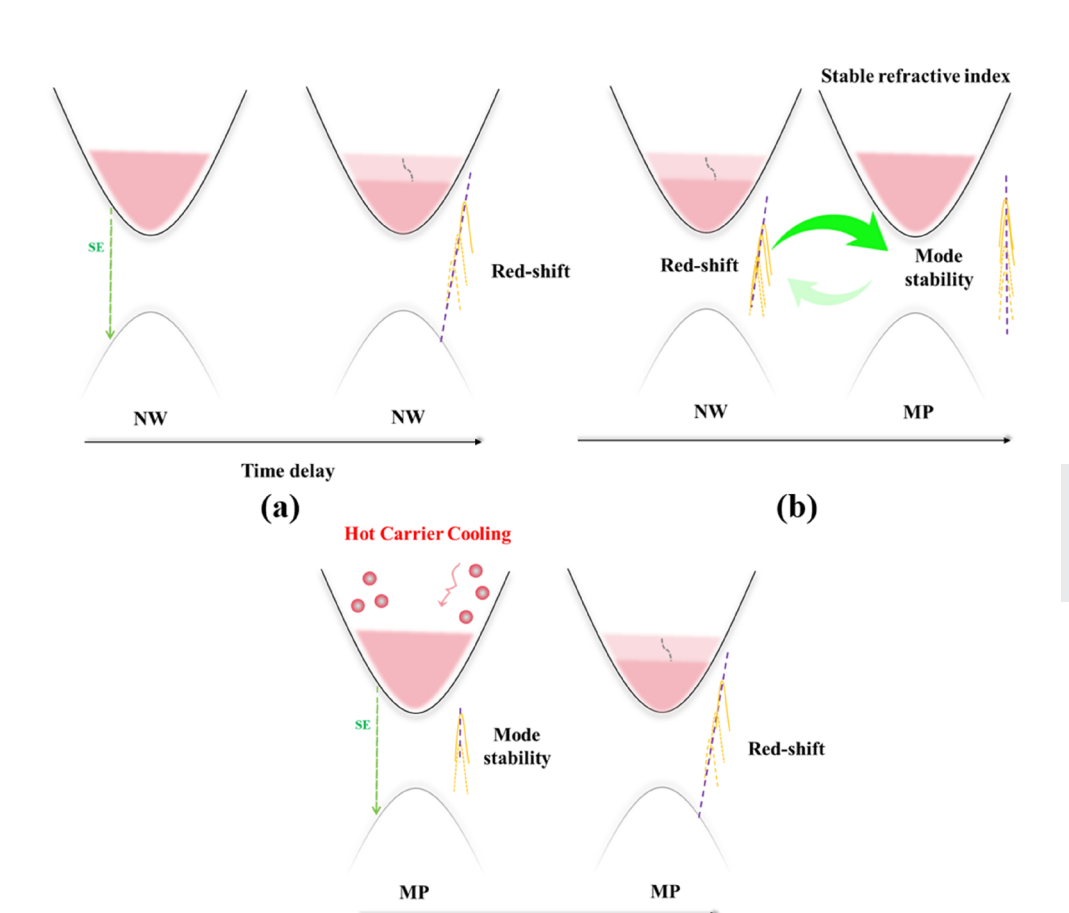


FIG. 4. (a) The spectral and time-resolved emission behavior of the composite as a function of pump fluence (21.7, 35.5, 54.4  $\mu$ J/cm<sup>2</sup>). (b) and (c) Emission intensity dynamics of the composite as a function of pump fluence. (d)–(f) Dynamics of the central wavelength in the composite at the low, medium, and high pump fluence.



(c)

**FIG. 5.** Schematic of dominant carrier behaviors affecting the transient mode shift in the composite at (a) low pump fluence, (b) medium pump fluence, and (c) high pump fluence.

and C are the corresponding amplitudes. The fitted curve, including the three separate components, can be illustrated in Figs. 2(d)–2(f). Transfers  $\tau_1,\tau_2$ , and  $\tau_3$  correspond to the BGR process, fast recombination lifetime, and slow recombination lifetime, respectively, and the calculated lifetimes are shown in Table S1 (supplementary material). The gradual increase in the BGR lifetime (0.65 ps < 1.05 ps < 1.58 ps) indicates that the BGR effect increases with increasing pump fluence, mainly due to the increase in carrier density.  $^{46-48}$ 

Furthermore, the absorption coefficient related to the refractive index is acquired by the Kramers–Kronig relationship. <sup>49</sup> The refractive index is inversely proportional to the excited carrier species during the laser emission. To explain the experimental phenomenon of BF and BGR competition-induced refractive index change process dependent on carrier density, one utilized a model to estimate the refractive index change induced by the excited carrier density. The global model related to the change in refractive index can be established as follows:  $\Delta \eta_{\rm BF+BGR}(\hbar \omega, N) = \left(\frac{\hbar c}{\hbar c}\right) \mathcal{P}\left[\int_{E_g'}^{\infty} \frac{\alpha_{\rm BF+BGR}(E_g'(N))}{E^2 - (\hbar \omega)^2} dE - \int_{E_g^0}^{\infty} \frac{\alpha(E_g E_g')}{E^2 - (\hbar \omega)^2} dE\right]$  (details in supplementary material), where h is the reduced Planck constant

supplementary material), where  $\hbar$  is the reduced Planck constant, c is the light speed,  $\mathcal{P}$  denotes the Cauchy principal value of the integral,  $\Delta \alpha_{BF+BGR}$  is the change in absorption coefficient by considering BF and BGR effects overall, which is a function of the

carrier density N and photon energy E,  $\Delta \eta$  is the change in refractive index. Employed by this model, the evolution of the refractive index change as a function of carrier density is shown in Fig. 3. In addition, the initial carrier density generated by the fs-pulsed laser was attained by the formula of  $N = (1-R)\frac{1}{d_p}\frac{F}{h\nu}(1-e^{-\alpha d_p}),^{50-52}$  where F is the pump fluence of a single pulse at excited energy, R is the reflectance,  $\alpha$  is the absorption coefficient, and  $d_p$  is the penetration depth. According to the pump fluence, the free carrier density N is  $2.74 \times 10^{18}$  cm<sup>-3</sup> at high pump fluence. Thus, the BF effect becomes dominant, resulting in a significant change in the refractive index at high pump fluence (see Fig. 3).

In light-emitting devices, photoexcited carrier processes such as electron-hole recombination and hot carrier dynamics, play a critical role in determining their optoelectronic performance. In addition, the application of OKG technology can detect rapid decay processes, providing a stage for the analysis of ultrafast laser dynamics. As shown in Fig. 4(a), one used micro-region OKG technology to study the time-resolved emission dynamics of the composite. As the pump fluence increases, there is a switch from the nanowire resonance mode dominated (high energy) to the microplate resonance mode dominated (low energy), and the laser rapidly decays over time, completing attenuation within 14 ps. Figures 4(b) and 4(c) show the PL emission dynamics above the threshold, with

an exponential decay in emission intensity. The decay process of this stimulated emission can be fitted by a mono-exponential function; the fitting lifetime ( $\tau$ ) is presented in Table S2 (supplementary material). The nanowire resonance mode has lifetimes of 3.725, 3.423, and 3.066 ps, and the lifetime of microplate resonance mode is 3.428, 3.373, and 4.631 ps as the pump fluence increases. The lifetime of the nanowire resonance mode decreases with increasing pump fluence due to the monotonic increase of carriers, leading to a faster-stimulated radiation process. For the microplate resonance mode, the lifetime first decreases (3.428-3.373 ps) and then significantly increases (3.373-4.631 ps) as the pump fluence increases. The abnormal increase in lifetime is due to the extended hot carrier cooling lifetime (i.e., a hot-carrier bottleneck effect, leading to enhanced nonradiative recombination), which further supports the dominant influence of the BF effect.53

Moreover, the ultrafast carrier dynamics of the composite are intricately linked to the laser characteristics. The position of the laser peaks at different pump fluences is cataloged in Figs. 4(d)-4(f). At low levels of pump fluence, the nanowire resonance mode wavelength undergoes a redshift over time, attributed to the decrease in carrier density; thus, a redshift happens in the resonance mode ( $\lambda_c/n_{eff}$  = constant). At medium levels of pump fluence, the microplate resonance mode increases monotonically within the first 4 ps and remains stable from 4 to 12 ps. The nanowire resonance mode increases monotonically after 4 ps. The constant resonant wavelength at different time delays is due to additional carriers compensating for those lost through stimulated emission, maintaining a stable refractive index.<sup>24</sup> At high levels of pump fluence, the resonance mode wavelength is nearly unchanged within 3 ps, then red-shift over time. One can construct a global physical model as shown in Fig. 5. The ultrafast energy transfer and hot carrier processinfluenced mode shift over time at different pump fluences can be explained. In the first few picoseconds, the main energy transfer can happen from microplate to nanowire (the significant BGR effect of nanowires compared to microplates).<sup>54</sup> With the recovery of the BGR process, the enhanced carrier number in the microplate maintains the balance of refractive index causing the microplate resonance mode to remain few changed during the long picosecond range. At high levels of pump fluence, the BF effect dominates, and the hot carrier cooling process participates in emission. Within the first 3 ps, the hot carrier cooling process can provide a buffer for adjustment of the energy level occupancy state, resulting in a small reflective index change caused by negligible transient mode shift. Then, the carrier density rapidly depletes with radiation recombination; therefore, the change in the refractive index becomes evident, and a redshift induced by the BF effect occurs.

# IV. CONCLUSION

One performed an experimental and theoretical investigation of CsPbBr3 monomer and composite micro/nanostructure by femtosecond TRPL and TA measurements for application in semiconductor-based microlasers. For the individual nanowire, the results demonstrate that the BGR effect causes the gain spectrum redshift, and the resonant mode blueshift is caused by the decrease in the refractive index of the individual resonant mode. For the composite, the TA spectrum manifests that the BF effect dominates at high levels of pump fluence, significantly influencing the refractive index during the laser emission. The energy transfer can affect the carrier density, resulting in few changes in the refractive index. In addition, the hot carriers cooling process is found to participate in stimulated radiation at higher levels of pump fluences, accompanied by an increase in the stimulated radiation lifetime. The hot carrier cooling process can provide a buffer for the adjustment of the energy level occupancy state, resulting in a small transient mode shift; however, the BF effect can cause a significant change in the refractive index as time increases. Our findings provide a foundation for controlling ultrafast laser emission via carrier dynamics, offering potential pathways for exploring high-performance materials in photonic microdevices.

#### SUPPLEMENTARY MATERIAL

The supplementary material contains a simplified illustration of the set-up for temporal-spatial-resolved microscopic optical Kerr-gate technology. XRD pattern of CsPbBr3 perovskites micro/nanostructure. Some laser characteristics are related to single nanowires and the composite structure.

#### **ACKNOWLEDGMENTS**

This work was supported by the National Natural Science Foundation of China (Grant Nos. 62175197 and 62027822).

#### **AUTHOR DECLARATIONS**

# **Conflict of Interest**

The authors have no conflicts to disclose.

#### **Author Contributions**

Canpu Yang: Data curation (equal); Validation (equal); Visualization (lead); Writing - original draft (lead); Writing - review & editing (equal). Yuheng Liu: Data curation (equal); Investigation (equal); Writing - review & editing (equal). Wenjiang Tan: Data curation (equal); Funding acquisition (lead); Resources (equal); Writing - review & editing (equal). Jinhai Si: Conceptualization (equal); Formal analysis (equal); Funding acquisition (equal); Investigation (equal). Xun Hou: Funding acquisition (equal); Methodology (equal); Project administration (equal).

#### **DATA AVAILABILITY**

The data that support the findings of this study are available within the article and its supplementary material.

### **REFERENCES**

<sup>1</sup>R. Chen, T. T. D. Tran, K. W. Ng, W. S. Ko, L. C. Chuang, F. G. Sedgwick, and C. Chang-Hasnain, "Nanolasers grown on silicon," Nat. Photonics 5, 170 (2011). <sup>2</sup>Z. Wang, X. Li, C. Chen, M. Lou, J. Wu, K. Gao, Z. Li, K. Sun, Z. Li, Z. Xiao, L. Li, P. Wang, S. Bai, J. Qiu, and D. Tan, "High relative humidity-induced growth of perovskite nanowires from glass toward single-mode photonic nanolasers at sub-100-nm scale," Adv. Sci. 12, 2412397 (2024).

- <sup>3</sup>Y. Fu, H. Zhu, J. Chen, M. P. Hautzinger, X. Y. Zhu, and S. Jin, "Metal halide perovskite nanostructures for optoelectronic applications and the study of physical properties," Nat. Rev. Mater. 4, 169 (2019).
- <sup>4</sup>L. Zhang, L. Mei, K. Wang, Y. Lv, S. Zhang, Y. Lian, X. Liu, Z. Ma, G. Xiao, Q. Liu, S. Zhai, S. Zhang, G. Liu, L. Yuan, B. Guo, Z. Chen, K. Wei, A. Liu, S. Yue, G. Niu, X. Pan, J. Sun, Y. Hua, W. Q. Wu, D. Di, B. Zhao, J. Tian, Z. Wang, Y. Yang, L. Chu, M. Yuan, H. Zeng, H. L. Yip, K. Yan, W. Xu, L. Zhu, W. Zhang, G. Xing, F. Gao, and L. Ding, "Advances in the application of perovskite materials," Nano-Micro Lett. 15, 177 (2023).
- <sup>5</sup>P. Li, Z. Zhou, G. Ran, T. Zhang, Z. Jiang, H. Liu, W. Zhang, Y. Yan, J. Yao, H. Dong, and Y. S. Zhao, "Spin-polarized lasing in manganese doped perovskite microcrystals," Nat. Commun. 15, 10880 (2024).
- <sup>6</sup>L. Lei, Q. Dong, K. Gundogdu, and F. So, "Metal halide perovskites for laser applications," Adv. Funct. Mater. 31, 2010144 (2021).
- <sup>7</sup>D. Chen, G. Zou, Y. Wu, B. Tang, A. L. Rogach, and H. L. Yip, "Metal halide perovskite LEDs for visible light communication and lasing applications," Adv. Mater. (published online 2024).
- <sup>8</sup>K. Elkhouly, I. Goldberg, X. Zhang, N. Annavarapu, S. Hamdad, G. Croes, C. Rolin, J. Genoe, W. Qiu, R. Gehlhaar, and P. Heremans, Nat. Photonics 18, 132 (2024).
- <sup>9</sup>Z. Gu, H. Gu, N. Zhang, S. Jiang, G. Wang, Y. Mao, J. Liao, S. Yang, C. Liang, and G. Xing, "Silicon-integrated perovskite photonic laser based on bound states in continuum," Laser Photonics Rev. 19, 2401327 (2025).
- <sup>10</sup> L. Lei, D. Seyitliyev, S. Stuard, J. Mendes, Q. Dong, X. Fu, Y. A. Chen, S. He, X. Yi, L. Zhu, C. H. Chang, H. Ade, K. Gundogdu, and F. So, "Efficient energy funneling in quasi-2D perovskites: From light emission to lasing," Adv. Mater. 32, 1906571 (2020).
- <sup>11</sup>X. Yu, J. Guo, Y. Mao, C. Shan, F. Tian, B. Meng, Z. Wang, T. Zhang, A. K. K. Kyaw, S. Chen, X. Sun, K. Wang, R. Chen, and G. Xing, "Enhancing the performance of perovskite light-emitting diodes via synergistic effect of defect passivation and dielectric screening," Nano-Micro Lett. **16**, 205 (2024).
- passivation and dielectric screening," Nano-Micro Lett. **16**, 205 (2024). <sup>12</sup>C. Zhao, J. Guo, J. Tao, J. Chu, S. Chen, and G. Xing, "Pulse-doubling perovskite nanowire lasers enabled by phonon-assisted multistep energy funneling," Light: Sci. Appl. **13**, 170 (2024).
- <sup>13</sup>G. Xing, N. Mathews, S. S. Lim, N. Yantara, X. Liu, D. Sabba, M. Grätzel, S. Mhaisalkar, and T. C. Sum, "Low-temperature solution-processed wavelength-tunable perovskites for lasing," Nat. Mater. 13, 476 (2014).
- <sup>14</sup>X. Liu, L. Niu, C. Wu, C. Cong, H. Wang, Q. Zeng, H. He, Q. Fu, W. Fu, T. Yu, C. Jin, Z. Liu, and T. C. Sum, "Periodic organic-inorganic halide perovskite microplatelet arrays on silicon substrates for room-temperature lasing," Adv. Sci. 3, 1600137 (2016).
- <sup>15</sup>Z. Xu, X. Han, W. Wu, F. Li, R. Wang, H. Lu, Q. Lu, B. Ge, N. Cheng, X. Li, G. Yao, H. Hong, K. Liu, and C. Pan, "Controlled on-chip fabrication of large-scale perovskite single crystal arrays for high-performance laser and photodetector integration," Light: Sci. Appl. 12, 67 (2023).
- <sup>16</sup>H. Zhu, Y. Fu, F. Meng, X. Wu, Z. Gong, Q. Ding, M. V. Gustafsson, M. T. Trinh, S. Jin, and X. Y. Zhu, "Lead halide perovskite nanowire lasers with low lasing thresholds and high quality factors," Nat. Mater. 14, 636 (2015).
- <sup>17</sup>Y. Wang, X. Li, V. Nalla, H. Zeng, and H. Sun, "Solution-processed low threshold vertical cavity surface emitting lasers from all-inorganic perovskite nanocrystals," Adv. Funct. Mater. 27, 1605088 (2017).
- <sup>18</sup>I. Goldberg, N. Annavarapu, S. Leitner, K. Elkhouly, F. Han, N. Verellen, T. Kuna, W. Qiu, C. Rolin, J. Genoe, R. Gehlhaar, and P. Heremans, "Multimode lasing in all-solution-processed UV-nanoimprinted distributed feedback MAPbI<sub>3</sub> perovskite waveguides," ACS Photonics 10, 1591 (2023).
- <sup>19</sup> A. P. Schlaus, M. S. Spencer, K. Miyata, F. Liu, X. Wang, I. Datta, M. Lipson, A. Pan, and X. Y. Zhu, "How lasing happens in CsPbBr<sub>3</sub> perovskite nanowires," Nat. Commun. 10, 265 (2019).
- <sup>20</sup>J. Wang, H. Yu, G. Liu, W. Liu, Y. Duan, X. Cheng, L. Dai, S. Wang, and Q. Gong, "Ultrafast lasing dynamics in a CsPbBr<sub>3</sub> perovskite microplate," Adv. Photonics Res. 3, 2100182 (2022).
- <sup>21</sup> W. Du, S. Zhang, Z. Wu, Q. Shang, Y. Mi, J. Chen, C. Qin, X. Qiu, Q. Zhang, and X. Liu, "Unveiling lasing mechanism in CsPbBr<sub>3</sub> microsphere cavities," Nanoscale 11, 3145 (2019).

- <sup>22</sup>G. Weng, J. Tian, S. Chen, J. Yan, H. Zhang, Y. Liu, C. Zhao, X. Hu, X. Luo, J. Tao, S. Chen, Z. Zhu, J. Chu, and H. Akiyama, "Electron–hole plasma lasing dynamics in CsPbCl<sub>m</sub>Br<sub>3-m</sub> microplate lasers," ACS Photonics **8**, 787 (2021).
- <sup>25</sup>M. He, Y. Jiang, Q. Liu, Z. Luo, C. Ouyang, X. Wang, W. Zheng, K. Braun, A. J. Meixner, T. Gao, X. Wang, and A. Pan, "Revealing excitonic and electronhole plasma states in stimulated emission of single CsPbBr<sub>3</sub> nanowires at room temperature," Phys. Rev. Appl. 13, 044072 (2020).
- <sup>24</sup>P. Ma, J. Si, L. Yan, J. Wu, J. Xu, and X. Hou, "Influence of hot carrier cooling and band-filling effect on linewidth of perovskite microlasers," Adv. Opt. Mater. 12, 2400189 (2024).
- <sup>25</sup> Z. Su, Z. Cao, F. Cao, Y. He, J. Zhang, G. Weng, X. Hu, J. Chu, H. Akiyama, and S. Chen, "Crystallization mechanism and lasing properties of CsPbBr<sub>3</sub> perovskites by chemical vapor deposition," Chem. Eng. J. 472, 144906 (2023).
- <sup>26</sup>Y. He, Z. Su, F. Cao, Z. Cao, Y. Liu, C. Zhao, G. Weng, X. Hu, J. Tao, J. Chu, H. Akiyama, and S. Chen, "Lasing properties and carrier dynamics of CsPbBr<sub>3</sub> perovskite nanocrystal vertical-cavity surface-emitting laser," Nanophotonics 12, 2133 (2023).
- <sup>27</sup>X. He, H. Gong, H. Huang, Y. Li, J. Ren, Y. Li, Q. Liao, T. Gao, and H. Fu, "Multicolor biexciton lasers based on 2D perovskite single crystalline flakes," Adv. Opt. Mater. 10, 2200238 (2022).
- <sup>28</sup> L. Polimeno, A. Coriolano, R. Mastria, F. Todisco, M. De Giorgi, A. Fieramosca, M. Pugliese, C. T. Prontera, A. Rizzo, L. De Marco, D. Ballarini, G. Gigli, and D. Sanvitto, "Room temperature polariton condensation from whispering gallery modes in CsPbBr<sub>3</sub> microplatelets," Adv. Mater. 36, 2312131 (2024).
- <sup>29</sup> H. Purwar, S. Idlahcen, C. Rozé, D. Sedarsky, and J. B. Blaisot, "Collinear, two-color optical Kerr effect shutter for ultrafast time-resolved imaging," Opt. Express 22, 15778 (2014).
- <sup>30</sup>C. Couteau, A. Larrue, C. Wilhelm, and C. Soci, "Nanowire lasers," Nanophotonics 4, 90 (2015).
- <sup>31</sup> X. Wang, H. Zhou, S. Yuan, W. Zheng, Y. Jiang, X. Zhuang, H. Liu, Q. Zhang, X. Zhu, X. Wang, and A. Pan, "Cesium lead halide perovskite triangular nanorods as high-gain medium and effective cavities for multiphoton-pumped lasing," Nano Res. 10, 3385 (2017).
- <sup>32</sup> Q. Zhang, R. Su, X. Liu, J. Xing, T. C. Sum, and Q. Xiong, "High-quality whispering-gallery-mode lasing from cesium lead halide perovskite nanoplatelets," Adv. Funct. Mater. 26, 6238 (2016).
- $^{33}$ L. Protesescu, S. Yakunin, M. I. Bodnarchuk, F. Krieg, R. Caputo, C. H. Hendon, R. X. Yang, A. Walsh, and M. V. Kovalenko, "Nanocrystals of cesium lead halide perovskites (CsPbX<sub>3</sub>, X = Cl, Br, and I): Novel optoelectronic materials showing bright emission with wide color gamut," Nano Lett. 15, 3692 (2015).
- <sup>34</sup>S. L. Chen, J. Stehr, N. K. Reddy, C. W. Tu, W. M. Chen, and I. A. Buyanova, "Efficient upconversion of photoluminescence via two-photon absorption in bulk and nanorod ZnO," Appl. Phys. B 108, 919 (2012).
- <sup>35</sup>X. Wen, R. Sheng, A. W. Y. Ho-Baillie, A. Benda, S. Woo, Q. Ma, S. Huang, and M. A. Green, "Morphology and carrier extraction study of organic–inorganic metal halide perovskite by one- and two-photon fluorescence microscopy," J. Phys. Chem. Lett. 5, 3849 (2014).
- <sup>36</sup>J. B. Khurgin and M. A. Noginov, "How do the Purcell factor, the Q-factor, and the beta factor affect the laser threshold?," Laser Photonics Rev. 15, 2000250 (2021).
- <sup>37</sup>R. Huber, F. Tauser, A. Brodschelm, M. Bichler, G. Abstreiter, and A. Leitenstorfer, "How many-particle interactions develop after ultrafast excitation of an electron–hole plasma," Nature 414, 286 (2001).
- <sup>38</sup>K. Wang, Z. Gu, S. Liu, J. Li, S. Xiao, and Q. Song, "Formation of single-mode laser in transverse plane of perovskite microwire via micromanipulation," Opt. Lett. **41**, 555 (2016).
- <sup>39</sup> K. Wang, S. Sun, C. Zhang, W. Sun, Z. Gu, S. Xiao, and Q. Song, "Whispering-gallery-mode based CH<sub>3</sub>NH<sub>3</sub>PbBr<sub>3</sub> perovskite microrod lasers with high quality factors," Mater. Chem. Front. **1**, 477 (2017).
- <sup>40</sup> K. Wang, C. Huang, Q. Ruan, Y. Zhou, Y. Chen, H. Liu, S. Xiao, and Q. Song, "Emission control in metal halide perovskite lasers," ACS Photonics 10, 2091 (2023).
- <sup>41</sup>B. R. Bennett, R. A. Soref, and J. A. Del Alamo, "Carrier-induced change in refractive index of InP, GaAs and InGaAsP," IEEE J. Quantum Electron. **26**, 113 (1990).

- <sup>42</sup>V. V. Yushkov, V. A. Sitnyansky, A. S. Shorokhov, and A. A. Fedyanin, "Analog optical correlation augmented by Mie-resonant metasurfaces," ACS Photonics 11, 2506 (2024).
- <sup>43</sup> J. Fu, Q. Xu, G. Han, B. Wu, C. H. A. Huan, M. L. Leek, and T. C. Sum, "Author correction: Hot carrier cooling mechanisms in halide perovskites," Nat. Commun. 9, 238 (2018).
- <sup>44</sup>N. Soetan, A. Puretzky, K. Reid, A. Boulesbaa, H. F. Zarick, A. Hunt, O. Rose, S. Rosenthal, D. B. Geohegan, and R. Bardhan, "Ultrafast spectral dynamics of CsPb(Br<sub>x</sub>Cl<sub>1-x</sub>)<sub>3</sub> mixed-halide nanocrystals," ACS Photonics 5, 3575 (2018).
- <sup>45</sup>R. R. Tamming, J. Butkus, M. B. Price, P. Vashishtha, S. K. K. Prasad, J. E. Halpert, K. Chen, and J. M. Hodgkiss, "Ultrafast spectrally resolved photoinduced complex refractive index changes in CsPbBr<sub>3</sub> perovskites," ACS Photonics **6**, 345 (2019).
- <sup>46</sup> E. Jung, K. Budzinauskas, S. Öz, F. Ünlü, H. Kuhn, J. Wagner, D. Grabowski, B. Klingebiel, M. Cherasse, J. W. Dong, P. Aversa, P. Vivo, T. Kirchartz, T. Miyasaka, P. H. M. van Loosdrecht, L. Perfetti, and S. Mathur, ACS Energy Lett. 5, 785 (2020).
- <sup>47</sup>K. Justice Babu, G. Kaur, A. Shukla, R. Saha, A. Kaur, M. Sachdeva, D. K. Yadav, and H. N. Ghosh, "Fast polaron formation and low carrier mobility in defect-free polyhedral CsPbBr<sub>3</sub> perovskite nanocrystals," ACS Photonics **9**, 969 (2022).

- <sup>48</sup> H. Yang, J. Li, Z. Wang, Y. Zhong, H. Yang, H. Dong, and L. Zhang, "Universal surface repairing strategy enabling suppressed auger recombination in CsPbBr<sub>3</sub> perovskite quantum dots for low threshold lasing in a superlattice microcavity," Adv. Opt. Mater. 12, 2400141 (2024).
- <sup>49</sup>W. Chen, B. Zhang, K. Tao, Q. Li, J. L. Sun, and Q. Yan, "Giant ab-plane birefringence in quasi-1D fibrous red phosphorus," Angew. Chem., Int. Ed. **63**, e202403531 (2024).
- <sup>50</sup> J. M. Richter, M. Abdi-Jalebi, A. Sadhanala, M. Tabachnyk, J. P. H. Rivett, L. M. Pazos-Outón, K. C. Gödel, M. Price, F. Deschler, and R. H. Friend, "Enhancing photoluminescence yields in lead halide perovskites by photon recycling and light out-coupling," Nat. Commun. 7, 13941 (2016).
- <sup>51</sup> Y. Jia, R. A. Kerner, A. J. Grede, B. P. Rand, and N. C. Giebink, "Continuous-wave lasing in an organic-inorganic lead halide perovskite semiconductor," Nat. Photonics 11, 784 (2017).
- <sup>52</sup>G. Mannino, I. Deretzis, E. Smecca, A. La Magna, A. Alberti, D. Ceratti, and D. Cahen, "Temperature-dependent optical band gap in CsPbBr<sub>3</sub>, MAPbBr<sub>3</sub>, and FAPbBr<sub>3</sub> single crystals," J. Phys. Chem. Lett. 11, 2490 (2020).
- <sup>53</sup>M. Li, J. Fu, Q. Xu, and T. C. Sum, "Slow hot-carrier cooling in halide perovskites: Prospects for hot-carrier solar cells," Adv. Mater. **31**, 1802486 (2019).
- <sup>54</sup>J. Yan, T. Jiang, Q. Liu, Z. Xiao, W. Zhang, H. Zhou, G. Wu, and Z. Chen, "Giant band-gap renormalization and morphology-tunable defect-assisted carrier recombination in CsPbBr<sub>3</sub> microstructures," ACS Photonics **10**, 3976 (2023).